J. Am. Soc. Mass Spectrom. (2017) 28:2635–2645
DOI: 10.1007/s13361-017-1784-y

RESEARCH ARTICLE

Automated Morphological and Morphometric Analysis of Mass Spectrometry Imaging Data: Application to Biomarker Discovery

Gaël Picard de Muller,[1] Rima Ait-Belkacem,[1] David Bonnel,[1] Rémi Longuespée,[2,3] Jonathan Stauber[1]

[1]ImaBiotech SAS, Parc Eurasanté, 885 rue Eugène Avinée, 59120, Loos, France
[2]Mass Spectrometry Laboratory (LSM), Systems Biology and Chemical Biology, GIGA-Research, University of Liège, Allée du 6 août 11, 4000, Liège, Belgium
[3]*Present Address:* Institute of Pathology, University of Heidelberg, Im Neuenheimer Feld 224, 69120, Heidelberg, Germany

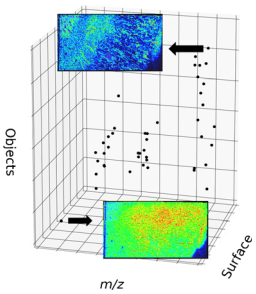

Abstract. Mass spectrometry imaging datasets are mostly analyzed in terms of average intensity in regions of interest. However, biological tissues have different morphologies with several sizes, shapes, and structures. The important biological information, contained in this highly heterogeneous cellular organization, could be hidden by analyzing the average intensities. Finding an analytical process of morphology would help to find such information, describe tissue model, and support identification of biomarkers. This study describes an informatics approach for the extraction and identification of mass spectrometry image features and its application to sample analysis and modeling. For the proof of concept, two different tissue types (healthy kidney and CT-26 xenograft tumor tissues) were imaged and analyzed. A mouse kidney model and tumor model were generated using morphometric – number of objects and total surface – information. The morphometric information was used to identify *m/z* that have a heterogeneous distribution. It seems to be a worthwhile pursuit as clonal heterogeneity in a tumor is of clinical relevance. This study provides a new approach to find biomarker or support tissue classification with more information.

Keywords: Mass spectrometry imaging, Computer vision, Data analysis, Quantitative analysis, Morphology

Received: 9 February 2017/Revised: 28 July 2017/Accepted: 10 August 2017/Published Online: 14 September 2017

Introduction

Mass spectrometry imaging (MSI) is the analysis of a sample by mass spectrometry in order to get a molecular mapping. This can be done using a variety of techniques [1]. Here we are interested in matrix-assisted laser desorption/ionization MSI (MALDI MSI) in which a rasterized sampling scheme for mass spectrum acquisition is used. For every set of coordinates (e.g., x, y), one gets a mass spectrum. In the MSI dataset, the coordinates and mass spectrum define a pixel if in 2D or a voxel if in 3D. Then, for each *m/z* value, generally using a binning, one gets an image specific to that *m/z* by considering all coordinates [2]. MSI and especially MALDI MS imaging has improved in recent years, mainly regarding the better spatial and spectral resolutions [3]. This makes it attractive in a number of fields, such as "omics" (mainly proteomics, metabolomics, and lipidomics) [4]. This technique may be used to understand biological pathways involved in different diseases and potentially support diagnostic or prognostic tests. Prior to data interpretation, MSI dataset analysis encompasses a number of analyses, including segmentation [5], classification [6], colocalization [7], quantitation [8], differential analysis [9], distribution in regions [10], heterogeneity [11], and molecular presence [12]. One of the strength of MSI is its potential for virtual microdissection [13], which allows the local analysis of biomolecules. However, users generally fall back to the average intensity for sample characterization and biomarker discovery. Thus, some low abundance or highly local molecules may depict the disease state, but could be hard to detect and identify as a marker of a specific state.

Electronic supplementary material The online version of this article https://doi.org/10.1007/s13361-017-1784-y) contains supplementary material, which is available to authorized users.

Correspondence to: Jonathan Stauber;
e-mail: stauber.jonathan@imabiotech.com

Morphological analyses have been used in histopathology [14], which is crucial for diagnostic and therapeutic decisions in many disease states. Semi-automated or fully automated methods can be used for morphometric analyses. Some staining implementations, such as immunostainings, allow the detailed morphometric analysis based on spatial relations [15].

To illustrate the point about localized molecules and learn from histopathology, the differential analysis of sample groups (e.g., disease versus control samples) has been considered for identifying biomarkers of interest. Theoretical cases where sample discrimination or markers of interest identification for a *m/z* image cannot be done by only evaluating the average intensity in a region have been recognized. The average intensity was held to be the same in both regions so another criterion to differentiate the two groups is needed. In Figure 1a, the case where a sample presents the same concentration of a targeted molecule with either a hotspot versus the case where multiple lower intensity hotspots are present is considered. In Figure 1b, the case where a sample presents a hotspot versus a bigger but lower intensity hotspot is present is considered. Three different cases were then considered where the intensity had the same dispersion in addition to the same central tendency. In Figure 1c, a small number of hotspots are distributed either throughout the tissue or preferentially in part of it. In Figure 1d, there is only one hotspot but it is either isotropic or not. In Figure 1e, the same number of isotropic hotspots with the same total and average surface are present but the hotspots have different individual surface.

The proposal of this study is to compute morphometric parameters using morphological image processing. The analysis of a binarized (segmented into background and foreground pixels, corresponding to black and white) molecular image would be able to discriminate the two groups. Measurements such as the number of objects (non-background connected groups of pixels) or those objects' average or total surface would differ. To consider that two non-background pixels are connected, we can use 4-connexity: a pixel can be connected either vertically or horizontally to another one but not diagonally. To compute the surface of a binarized image in pixels, the number of foreground pixels was used. To compute the number of objects, one moved across all pixels in the image, then if the current position is a foreground pixel, it has been set and all the foreground pixels connected to it (with 4-connexity) to the background value. The number of objects is equal to the number of times objects were set to the background value. In order to obtain binarized imaged, a global threshold can be applied using Otsu's method. Otsu's method automatically determines the best threshold as the one that minimizes the

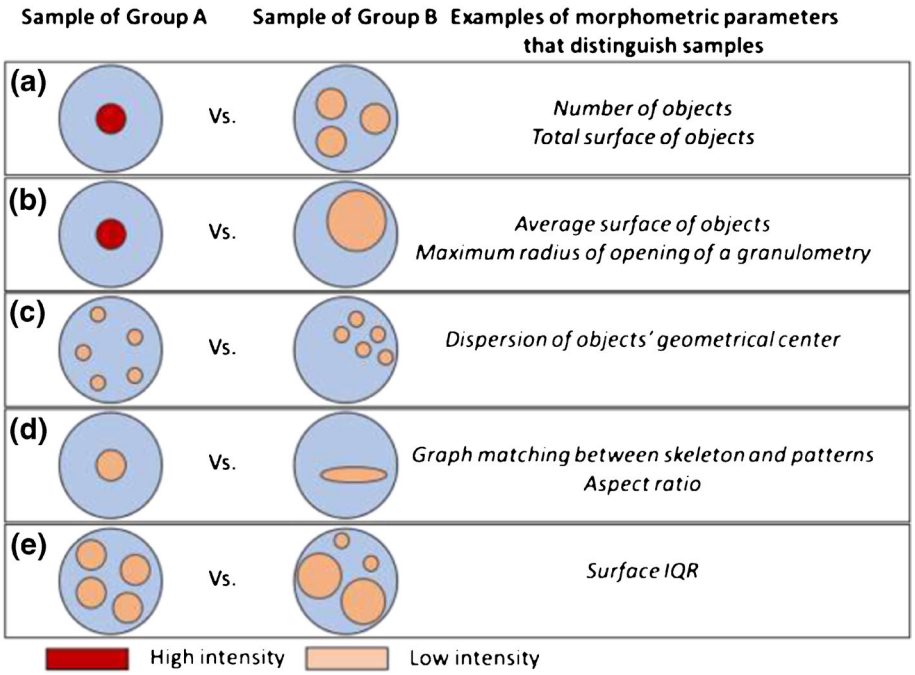

Figure 1. Theoretical cases within which sample discrimination or markers identification cannot be done by only evaluating the regional average intensities. **(a)** Case where a sample presents the same concentration of a targeted molecule with either a hotspot versus the case where multiple lower intensity hotspots are present and suggestion using the number of objects or the total number of objects to discriminate the two samples. **(b)** Case where a sample presents a hotspot versus a bigger but lower intensity hotspot and suggestion to use the average surface of objects or the maximum radius of opening of a granulometry, a virtual sieve to discriminate the two samples. **(c)** Case where a small number of hotspots are distributed either throughout the tissue or preferentially in part of it and suggestion to use the dispersion of object's geometrical center. **(d)** Case where there is only one hotspot but it is either isotropic or not and suggestion to use a graph matching approach or the aspect ratio to discriminate the two samples. **(e)** Case where the number of hotspots is the same as the total and average surface but with different individual surface and suggestion to use the surface IQR to distinguish the two samples

intra-class variance, which is the same as maximizing inter-class variance – the idea being that there are two kinds of pixels, foreground and background pixels, following different unimodal distributions. In more details, Otsu's method for image thresholding is an exhaustive search for the threshold value minimizing the sum of weighted intraclass variability; the weight being the probability of being in that class and the intraclass variability being the variance of the values assigned to that class. It is known to give imperfect results when an image does not have a bimodal histogram yet has been found effective in binarizing real world images [16].

For Figure 1a, the number of object or the total surface would separate the two cases. For Figure 1b, the average surface of an object would work but it would also be possible to calculate a granulometry [17] on each non-binarized image to distinguish them. A granulometry determines the size distribution of objects using a series of morphological opening operations, a kind of virtual sieving. As such, a granulometry does not require defining the segmentation prior processing. In the case of Figure 1c, the mean and standard deviation of the objects' geometrical center can be used. This allows expressing the positions in real world units. For Figure 1d, a graph matching between the object's skeleton and standard patterns (e.g., if one has a set of shapes to recognize) or more simply the aspect ratio (e.g., if one is measuring a deformation) would separate the two cases. Finally, for Figure 1e, the interquartile range (IQR) measures the dispersion of the object surfaces.

While intensities can solve some problems, for instance by considering their standard deviations, the same situation can arise with dispersion. Another class of features that might have helped to solve the situation is textural features. Textural features are features containing information about the spatial distribution of tones (e.g., coarseness, contrast). For instance, grey level co-occurrence matrices describe the co-occurrence of values over the image for some offset and are useful for the computation of textural features, for example by computing a global contrast. However, in spite of interesting results, and at least since Robert M. Haralick defined a set of features that are eponymously named [18], the pathophysiologic interpretation of textural features is still unclear [19].

For these reasons, we propose to include image analysis in the workflow of MSI datasets investigation. In this study, an additional analysis of MSI datasets using *m/z* images is performed. That step uses the MSI for further treatment and/or measurement. Figure 2 summarizes the evolution suggested. It shows how this step happens after having chosen the regions of interest. However, this is a simplification as the region selection can be refined during the image processing and analysis (e.g., using active contours [20]). Moreover, processing the image without extracting new parameters may help improve the final model (e.g., by applying a median filter to reduce the salt-and-pepper noise that could bias a mean).

First, this workflow is applied to generate models on a healthy kidney and CT-26 xenograft tumor model. The murine CT-26 model is a mouse colon carcinoma line [21], resulting in a rapidly growing grade IV carcinoma that is easily implanted and readily metastasizes. The CT-26 colon carcinoma is one of the most commonly used cell lines in drug development for developing and testing immunotherapeutic concepts, for instance when investigating biomarkers in colon malignancy. Second, the intelligibility of the measures is used for the selection of *m/z* presenting a heterogeneous distribution in the tumor tissue.

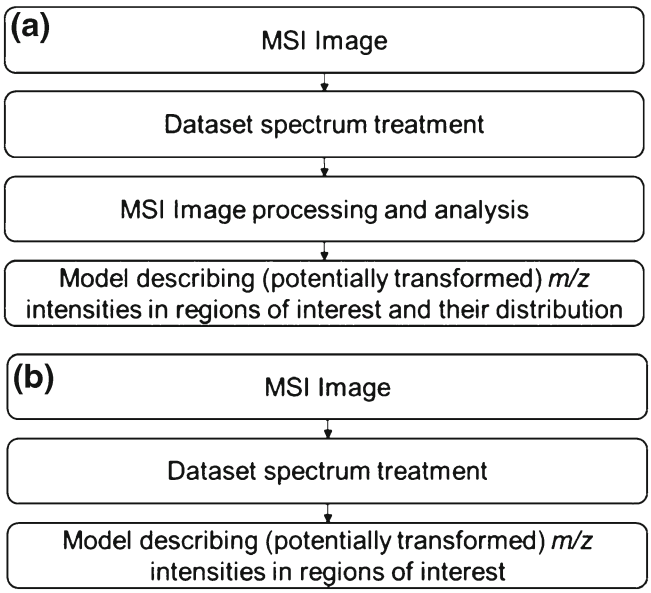

Figure 2. Comparison of the proposed MSI workflow with the standard one. **(a)** Displays the addition of an MSI image processing and analysis step that is not present in **(b)** the standard one. The dataset spectrum treatment step potentially includes spatial information (e.g., PCA) and region of interest determination (e.g., entire slide, visually, using segmentation or multivariate techniques). The MSI image processing and analysis is placed after spectrum treatment step because they generally are higher-order treatment (e.g., median filter) but some of them might be done before or between dataset spectrum treatments (e.g., region selection)

Experimental

Chemicals and Reagents

All chemicals, including 1,5-diaminonaphtalene (1,5-DAN), 9-aminoacridine (9-AA), acetonitrile (ACN), methanol, LC-MS water, and trifluoroacetic acid (TFA) were purchased from Sigma-Aldrich (St. Louis, MO, USA). Indium-tin-oxide (ITO) coated glass slides were purchased from Bruker Daltonics (Bremen, Germany).

Sample Collection and Tissue Preparation

BALB/c mice were inoculated subcutaneously with 1000 CT-26 cells. CT-26 is an N-nitroso-N-methylurethane-(NNMU) induced, undifferentiated colon carcinoma cell line. After tumor growth, mice were sacrificed by cervical dislocation and organs (kidney) and transplanted tumor were dissected, extracted, and snap frozen in liquid nitrogen for 15 s. The samples

were kept at –80 °C until use. Sagittal tissue sections of 10 µm were obtained using a cryostat microtome (CM-3050S; Leica Biosystems, Weitzlar, Germany) with a microtome chamber and a specimen holder chilled at –17 °C. The slices were thaw mounted onto ITO coated slides for downstream MALDI imaging.

All animal experiments were compliant with the 2010/63/UE European Directive on Laboratory Animal Welfare and were approved by an Ethical Committee (Animal Welfare Body from the BUC CMMI Animal Facility in Gosselies, Belgium. Animal Welfare Body Agreement number: LA 15005-18, Research Project Agreement number: BUC 2016-02, and BUC 2015-05).

For MALDI MSI of lipids and metabolites on kidney and tumor sections, a uniform layer of 1,5-DAN matrix (10 mg/mL with 50/50 ACN/H_2O 0.1% TFA) and 9-AA matrix (10 mg/mL prepared in 70% MeOH) were deposited using the sublimation procedure and the SunCollect device (SunChrom GmbH, Friedrichsdorf, Germany, one layer at 10 µL/min, one layer at 20 µL/min, and three layers at 35 µL/min), respectively.

MALDI-FTICR Imaging

MALDI MSI of lipids and metabolites was performed using a 7 T MALDI FT-ICR (SolariX, Bruker Daltonics, Bremen, Germany) with a SmartBeam II laser. MSI data were recorded in positive ion mode (kidney sagittal tissue section, 1,5-DAN, *m/z* range 100–1000 at 20 µm of spatial resolution with an on-line calibration) and negative ion mode (tumor tissue, 9-AA matrix, *m/z* range 50–1000 at 70 µm pixel size with an on-line calibration). The online calibration was a shift automatically applied by the instrument to the *m/z* axis to align the main matrix peak (y2 = y1 + s, 1,5-DAN: 159.091675, 9-AA: 193.07712, minimum intensity: 1 × 105, maximum distance: 30 ppm).

Data acquisition, processing, and data visualization were performed using the Flex software suite (ftmsControl 2.1.0, FlexImaging 4.1, and DataAnalysis 4.2) from Bruker Daltonics and Multimaging 1.1 (ImaBiotech SAS, France). MSI data were acquired from each tissue section as well as matrix control areas adjacent to the tissue sections to check for analyte dispersion during sample preparation.

Histological Staining and Digital Scan Image

Adjacent slices were obtained at the same time and stained with hematoxylin and eosin (H&E) solution. High-resolution histological images were then recorded using a digital slide scanner (3D Histech Pannoramic).

Data Processing Workflow

Analyses were done using custom python scripts. Plots were made with matplotlib [22]/seaborn (DOI:10.5281/zenodo.54844). For marker identification, the METLIN [23] database has been used with the following parameters: 3 ppm of mass accuracy, negative mode, and with the adducts $[M–H]^-$, $[M–H_2O–H]^-$, and $[M+Cl]^-$.

Kidney The 1000 most intense apexes of the mean spectrum of the acquisition were used to generate peaks with a tolerance of 10 ppm. The 10 ppm binning was done because peaks at higher *m/z* are wider. The choice of 1000 peaks was motivated by the length of the list of proposed peaks in DataAnalysis (962 *m/z* intervals) rounded to the nearest hundred. The simpler apex method was used to ensure some peaks that were visually identified were taken. As a visual inspection of the spectrum showed peaks had a close to Gaussian shape, the apex was considered sufficiently accurate (the centroid or an interpolating cubic spline's maximum were considered). For each peak, a linear greyscale gradient with 256 levels after application of a threshold of 1×10^6 arb.unit was created. This allowed the generation of images from the spot's values for visualization and validation of the processing. Masks (bit patterns arranged in the form of two level images that are used to extract information from specific zones in the original set of molecular images) for the pelvis, medulla, and cortex were generated on the basis of contrast ions (*m/z* having a discrete distribution that highlight an underlying histological region). The regions were confirmed by co-registration to the H&E stained slice.

After binarization by Otsu's method (determination of the threshold separating the dataset in two while minimizing the intra-class variance), objects having a surface less than 4 pixels (1600 square micrometers) were deleted. The masks were then used to isolate each region before measure. Finally, the regions' measurements were compared after normalization by their total surface.

Tumor The 200 most intense apexes of the mean spectrum of the acquisition were used to generate peaks with a tolerance of 10 ppm. As noise images were present with the first 1000 apexes, the number of apexes considered were reduced to 200. This reduction limits the amount of noise used as input during model construction. The value of each position was exported. Then a low threshold of 1×10^6 arb. unit was applied. Masks for the necrosis and proliferation regions were generated on the basis of contrast ions. These masks were used to isolate each region before binarization by Otsu's method. After binarization, objects having a surface less than 4 pixels (19 600 square µm) were deleted prior to measurements.

Results and Discussion

Kidney

As a proof of concept, a description of the molecular morphometric information of a control kidney section was performed and the obtained information was analyzed. In order to extract image features of each *m/z* value of the kidney, MSI was performed followed by data processing. First, the peak picking method was applied. The mean spectrum's slope was used to list maxima and their values. The 1000 highest ones with a tolerance of 10 ppm were then kept.

MS image treatment started with a low threshold at 1×10^6 arb. unit to eliminate most noise (visually determined by mean spectrum inspection). It was followed by a projection to a displayable format (256 grey level images) for ease of visual validation and to decrease the number of noise images.

The entire image was then binarized using Otsu's method. A first treatment of those binarized images consisted in deleting the objects having a surface less than 4 pixels (1600 μm2). This was done because even after the 1×10^6 arb. unit threshold, some noise was still present. The imaging technique is known to cause hotspots [24]; the 4 pixels threshold was used to delete those artefactual objects that would have biased the analysis. Visual inspection of a random sample of binarized images showed that this high intensity noise was unlikely to occur in more than three sequentially connected positions and, due to the image spatial resolution, objects were not made of less than 4 pixels. Based on contrast ions/histology, masks were then applied to the pelvis, medulla, and cortical regions, Figure 3a. As the tissue was heterogeneous, the *m/z* behavior in these substructures was expected to differ somewhat, which was seen as of interest.

Out of the 1000 initial images, 782 were kept as they held variability (pixels in both foreground and background) at the chosen thresholds (intensity, minimal surface). The number of objects and the total surface were computed for the three regions associated with each molecular image. As shown in Figure 3a, a sagittal section was used where the pelvis had the smallest surface followed by the cortex. The number of objects was compiled with the total surface for each *m/z* image that held information in Figure 3b. Pelvis, medulla, and cortex images had an average surface of 167.34 pixels (SD: 394.55), 1148.45 pixels (SD: 2 513.92), and 440.91 pixels (SD: 1 139.48), and an average number of objects of 4.21 (SD: 9.1), 35.82 (SD: 62.45), and 21.93 (SD: 40.51) in their respective regions.

The image surfaces normalized by the total area in pixels (respectively 1905, 16 278 and 11 126 for the pelvis, medulla, and cortex) were used to check our initial assumption that the regions had different values. The normalization was done to make the measurements of regions of different sizes comparable. The 2-tailed Welch's *t*-test with Bonferroni correction were used for multiple comparisons. We failed to find evidence for differences in the mean number of objects between the three regions or in mean surface between medulla and pelvis. However, significant differences in surfaces were found between the medulla and the cortex ($n = 782$, $t = 4.66$, $p < 1 \times 10^{-3}$) and between the pelvis and the cortex ($n = 782$, $t = 5.83$, $p < 1 \times 10^{-3}$).

In order to check that the workflow produced the expected kind of results, it was verified that a positive correlation between the maximum number of objects and the maximum surface does exist in the three regions ($r > 0.999$, $p < 0.05$). A high region surface is easily split in a high number of objects. In Figure 3b, at the lower left end, there were very few objects and those objects were small. Such images corresponded to a single hotspot. Then as the number of objects increased, even if they had the same individual surface, the cumulated surface increased. Finally, as the objects merged, the number of objects diminished again while the surface increased until there was only one spot covering almost the entire image. Supplementary Figure SI1 zooms in the pelvis points and four *m/z* images are shown to help understand how the axes interact.

Of course, the number of objects and the objects' surface only give a high-level view of each *m/z* image and not the whole morphology. But even with these simple measurements, it is possible to go further such as by estimating the probability density function (pdf) of the objects' surface. Figure 4a shows the violin plots of the objects' surface in the medulla region for two images having a close surface value but a different number of objects in this region. The two object surface distributions seem to differ. Visual inspection of the distributions in Figure 4b confirms it. The pdf can be the basis of other studies using, for instance, the two sample Kolmogorov-Smirnov test to check the hypothesis that two images have the same underlying distribution of object size.

Overall, this method enables the creation of the basis for a model: using a kidney, it allows one to describe peaks in terms of intensity, surface and number of objects in three sub-regions of sagittal kidney sections. Next would be the analysis of more slices representing the same part of the kidney in different samples to assess variability.

Tumor

The tumor was a xenograft initially composed of a few colon carcinoma CT-26 cells, which were allowed to grow, then harvested. Potential markers of heterogeneity have been investigated in necrosis and proliferative regions.

A morphological workflow was applied for a tumor section similar to the one used for the kidney section. This was done because heterogeneously distributed molecules in the tumor microenvironment are of high interest to clinicians [25]. The morphological analysis of each *m/z* value may help identify those heterogeneously distributed molecules by their *m/z* images.

In the tumor sample case, the kidney procedure was followed albeit with a few differences. The number of peaks considered was reduced in order to input less noise during model generation. The masks mainly represented the proliferative and necrosis regions. The masks were applied before Otsu's method. These masks allowed the analysis of each region to give a more robust description of the distribution for both, as each was based on the region's intensities/features with less influence from the other. In other words, a noise threshold that could be different between the regions was determined. The intensity set was not reduced to 256 values but kept as it is (thousands of unique values). Not grouping values allows a better calculation of the variances. Otsu's method was applied to the non-null values in order to only use the acquired values we deem not to be noise. Only true heterogeneity, not the random noise's heterogeneity, was of interest. We computed the surface and the number of objects for both regions as they were tumor. This

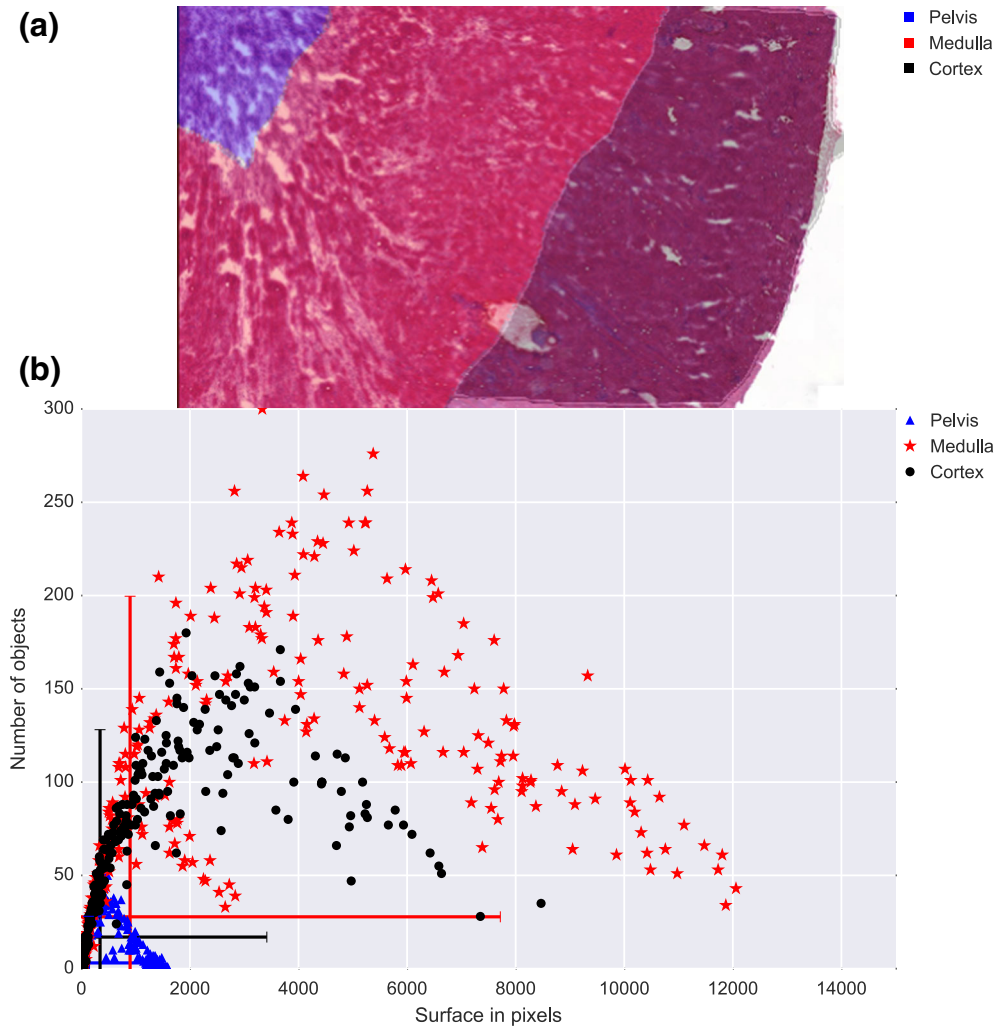

Figure 3. Overview of the kidney dataset with the three histological regions and the *m/z* associated to regions number of objects and surface measurements. **(a)** Adjacent H&E stained kidney section used for the creation of masks with the pelvis region in blue, the medulla region in red, and the cortex region in black, and **(b)** scatterplot of the *m/z* images along the total surface and the number of objects in the associated region. The region's *m/z* occupy roughly a negative parabola. The lower left parts are images having a few small hotspots. The middle part with varying number of object exemplifies how a surface measurement can be reached with few objects of relatively high surface or more objects of a smaller surface. The lower right parts are images having few but large objects

led to obtaining the basis of a model combining the number of object and surface information in the two regions.

As a starting point, measures of the central tendencies and dispersions of the surface and the number of objects for this tumor were computed. The 200 *m/z* ions had an average surface of 339.685 pixels out of 3941 or 8.62% of coverage (SD: 457.87 pixels, 11.6%) and 816.125 pixels out of 6426 or 12.7% of coverage (SD: 924.08 pixels, 14.38%) in the necrosis and proliferative region, respectively. They had an average number of objects of 14.88 (SD: 16.51) and 22.845 (SD: 19.41) in the necrosis and proliferative region, respectively. In other words, the average image has around 10% coverage in each region with 15 objects in the necrosis region and 23 objects in the proliferative region. As the surface and the number of objects are natural numbers, we can say that the variability mostly came from images having higher than average values for these parameters. Beyond the general description of the pattern, working on individual *m/z* ions is also possible and classes could be determined on the basis of morphometric parameters (e.g., heterogeneous *m/z*). Moreover, this approach could be used to identify which molecules change between conditions.

Looking for heterogeneous *m/z*, the sum of the standard score from each region was analyzed. This allowed taking into account both regions of the tumor equally. Peaks tended to have a surface proportional to the number of objects, and values were almost evenly distributed along the *m/z* axis. This gave an opportunity to discover a lower number of detected peaks between *m/z* 500 and 600 compared with the rest of the axis. The *m/z* axis did not appear to be relevant for heterogeneity analysis as any molecule may be of interest. Both those that had a small or a high surface were

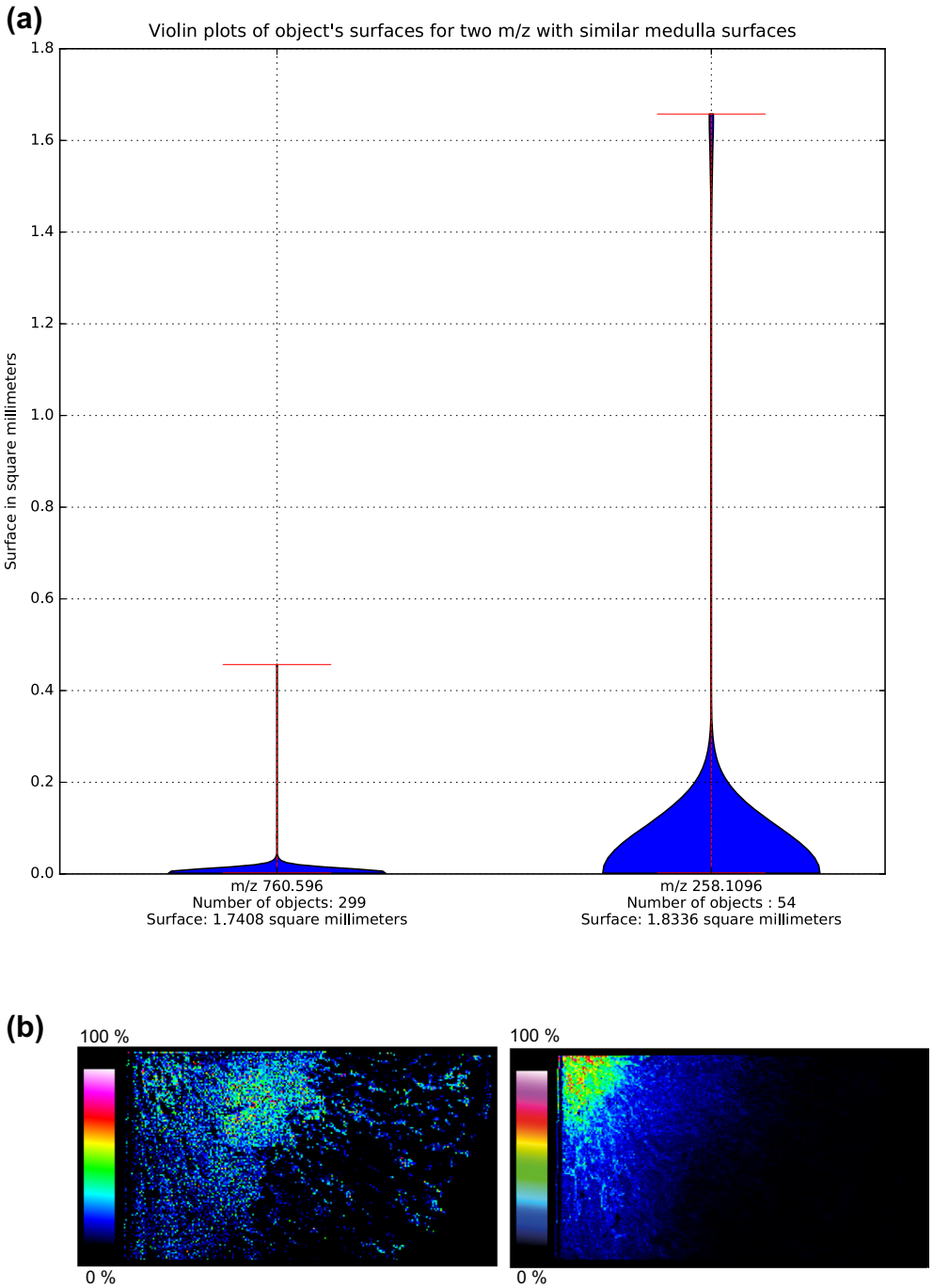

Figure 4. Example of distribution differences between two *m/z* of similar surfaces but different number of objects for the medulla region. **(a)** Violin plots estimating the probability density function of object's surface (Gaussian kernel, extrema indicated by bars) and indications about the number of objects and total surface measured (fold change close to 1 for the surface, fold change of more than 5 for the number of objects) for *m/z* 760.596 and *m/z* 258.1096, and **(b)** the molecular images associated to the same *m/z* 760.596 and *m/z* 258.1096 having very different distributions

excluded. Both empty (black) and full (white) images are homogeneous. Furthermore, the objective was to have a number of objects not too far from the mean. Otherwise we might have taken either single hotspots or cases where the number of objects was so high that their distribution over the image was homogeneous. We formalized this description as saying that points having a sum of standard score for the two regions between 1 and 3 for the surface and –1 and 1 for the number of objects were potentially heterogeneous *m/z*. With these criteria, five heterogeneous *m/z* in the scatterplot of the sum of the standard scores for both regions were selected (*m/z* 186.0456, *m/z* 268.8005, *m/z* 295.0264, *m/z* 391.2259, *m/z* 417.2419).

After interrogation of an open-source metabolomics database with a 3 ppm tolerance (METLIN, https://metlin.scripps.

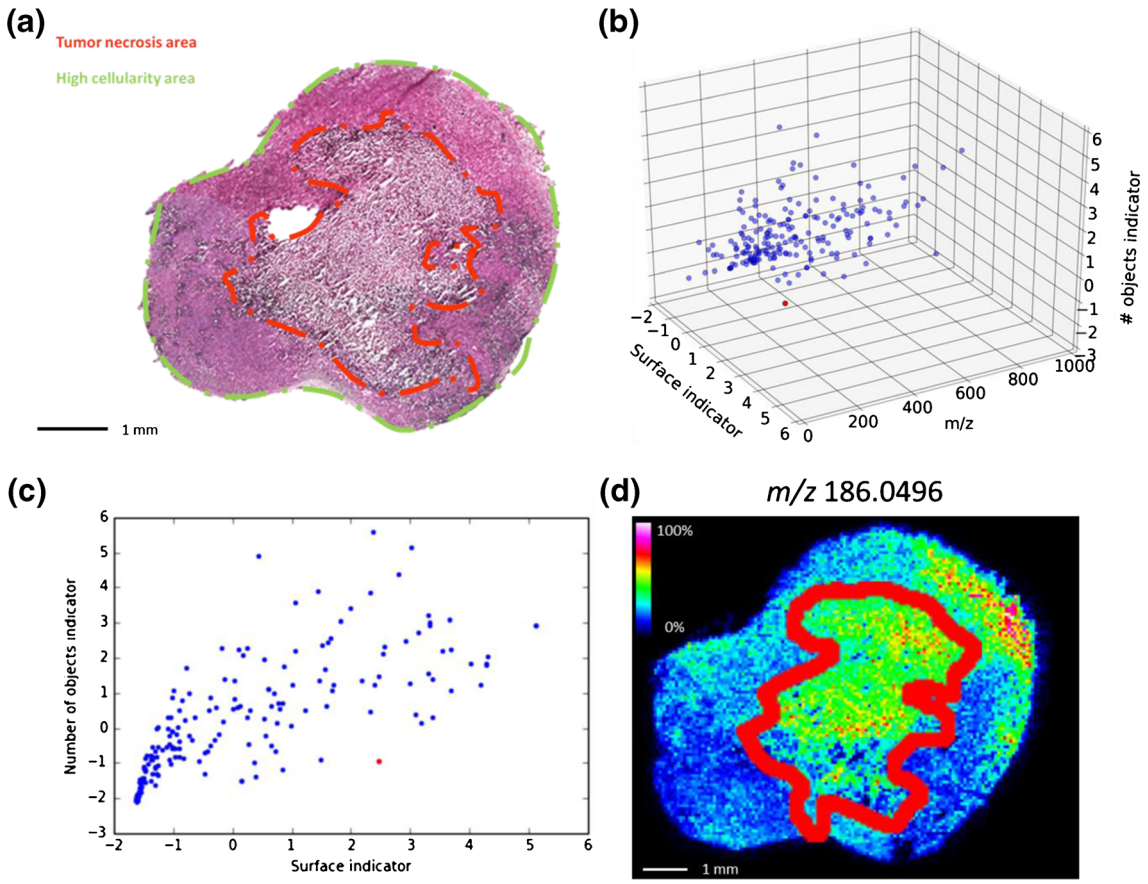

Figure 5. Visual of the key steps leading to the selection of heterogeneously distributed *m/z*. **(a)** H&E staining of a slice adjacent to the one used for imaging with the two regions of interest identified, **(b)** 3D scatterplot of the sum of the standardized surface and number of objects for each *m/z*, the points (*m/z*) appear regularly spaced on the *m/z* axis, a point of interest for its low number of objects but high surface (heterogeneous *m/z*) is shown in red, **(c)** 2D scatterplot of the sum of the standardized surface and number of objects for each *m/z*, a point of interest for its low number of objects but high surface (heterogeneous *m/z*) is shown in red, **(d)** molecular image of the previously selected point of interest (heterogeneous) *m/z* 186.0496 showing a high surface with few objects

edu/), *m/z* 186.0456, *m/z* 268.8005 and *m/z* 295.0264 did not give relevant hits while *m/z* 391.2259 and *m/z* 417.2419 were putatively identified as 3-oxochola-1,4,6-trien-24-oic acid and arachidonoyl-1-thio-glycerol lipids, respectively, (multiple possible identification at the specified measure error).

The *m/z* 186.0496 had the highest surface for the lowest number of objects of the five, which would facilitate visual validation [intensity: 1688 772 (SD: 734,593), intensity in the proliferative region: 1,378,544 (SD: 645,402), intensity in the necrosis area: 1,926,854 (SD: 675,343)]. It was validated as

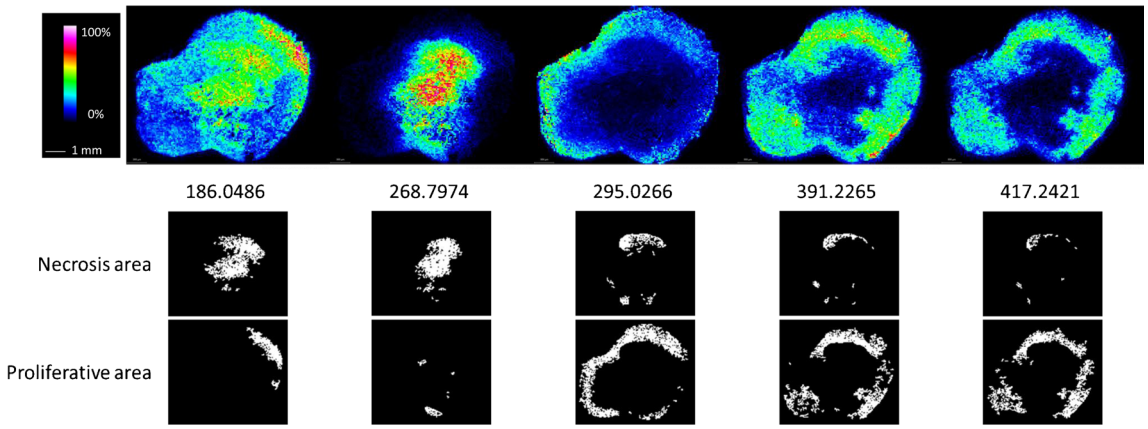

Figure 6. Images associated with the heterogeneously distributed *m/z*. Molecular images that show the heterogeneity are presented (top) along with the two associated binarized images (bottom) highlighting both necrosis and proliferative areas

peak by opening the mean image spectrum in DataAnalysis (SNR: 8215.2, automatically detected). Figure 5a shows an H&E stained section adjacent to the imaged one and. Figure 5b shows the distribution of the data points in the 3D space based on the scores for surface and number of objects and *m/z*. Figure 5c is the projection of the 3D data points along the surface score and number of objects score axes. Figure 5d is the image associated with the *m/z* 186.0486. It can be observed that it is heterogeneously distributed in both regions, mostly present in the upper part of the necrosis region and in the upper right part of the proliferation region. So, using this approach, a potentially interesting *m/z* that may help to characterize an intra-tumor heterogeneity pattern inside the necrosis and proliferative regions rather than between them was found.

The five MS images fulfilling the criteria are presented along with the two associated binarized images in Figure 6. It can be observed that for the necrosis area, *m/z* 186.0456 and *m/z* 268.8005 were similarly anti-localized compared with *m/z* 295.0264, *m/z* 391.2259, and *m/z* 417.2419. The proliferation region of *m/z* 186.0456 is highlighted in the top right corner as the most intense part of the image. The proliferation region of *m/z* 268.8005 seemed to indicate a region close to the necrosis area. The proliferation region of *m/z* 295.0264 was very widespread but with separated parts and lacked the rightmost part that was visible in the image of *m/z* 417.2419. The proliferation regions of *m/z* 391.2259 and *m/z* 417.2419 were very similar.

It can be imagined that the histological localization of this ion of interest and even others could translate one of the tumoral heterogeneity features. This intra-tumoral modeling of proliferation and necrosis extent would certainly be important to understand both the natural history of neoplasms and the selection of test samples for reliable analysis during diagnosis, prognosis, and monitoring treatment response. A concrete example of application of morphological analysis would be monitoring the evolution of the presence of marker compounds in cancerous tissues from patients before and after therapy. The action of an anticancer treatment might influence the repartition of compounds in tumors, depending on the variety of different cancer cell clones within the tumor. Some morphometric parameters could then stand as markers of drug action.

Workflow Considerations

In the kidney and tumor cases, the principal limitation identified was the use of the global Otsu's method for pixel assignation to background or foreground. Its assumption of a bimodal histogram over the entire image was not always met. Other segmentation methods may be of interest as they generate labeled images that can be analyzed as objects of different natures rather than groupings of positions per similarity. Alternatives to the global Otsu's method for object detection deserve consideration for future applications. For instance, applying the local (that will identify local in addition to global hotspots) and/or multilevel (that may identify the distribution of interest if there are more than two underlying object classes) version of Otsu's method or balanced histogram thresholding might be useful. A completely different method such as those based on watersheds or active contours may be of interest when thresholds need more adaptation to local conditions than is provided by the local versions of Otsu's method or balanced histogram thresholding. Even with these limitations, tissue classification and biomarker detection could benefit from this approach.

The peak picking method was very simple but prone to false positives (particularly in the case of peaks with shoulders), and some peaks might overlap. Less than 2.5% of the peak overlapped and around 1% of the peak's overlap included another apex.

The threshold of 1×10^6 arb. unit was chosen on the basis of a visual examination of the datasets. It was used to quickly denoise images. However, not all images were affected the same way. Image peaking techniques with a local binarization method seem to be a good alternative to this thresholding. Histograms and binarized images were examined with or without this threshold. This thresholding had a limited impact on the threshold determined by Otsu's method. This is because the threshold only suppressed the lower end of the noise. As there was still noise and signal, Otsu's method gives a similar result.

The minimum surface was chosen primarily because of the observed noise. Some MS processing could have helped reduce or eliminate the need for this surface threshold by reducing the amount and the intensity of the noise. First among them, normalization could have reduced some of the analytical variability. However, in the kidney case, spectrum normalization was not feasible as supposedly some measurements will stay the same in different anatomical structures, which was considered a priori wrong. For instance, the TIC normalization relies on the total ion count (approximately the chemical information) being similar and the RMS normalization relies on the signals of high intensity being similar. In the tumor case, the surface threshold developed for the kidney case was considered to be a good enough alternative to normalization for this application. As we were interested in many molecules, an internal standard approach was not feasible.

The simple descriptive models generated were meant to give a summary of the sample across multiple molecules. Minute changes in only one molecule may not be detected with such summaries. However, limited changes along many molecules may be detected that way.

As the goal is to make a model, reproducibility must be mentioned. Reproducibility issues arise due to bioanalytical variability. The bioanalytical variability is expected to create some variability in the morphological MSI analysis. The biological variability is expected to be the main source of variability. The analytical variability is expected to change only a few pixels in the binarized image as its impact relates more to single pixel hotspots and intensities than to separatability. However, the bioanalytical variability has not been assayed and needs to be investigated in the near future.

Conclusion

In this study, an additional analysis for the investigation of MSI datasets with a focus on the molecular images' features was presented. Interestingly, the morphological analysis has the advantage of being quantitative. The extracted information can be used in many contexts, including image peaking, classification, or differential analysis. This was applied to two proof-of-concept studies: kidney and tumor description and intratumoral heterogeneity detection. The former showed that one could differentiate regions on the basis of the ion distributions. The latter is of particular interest as tumor heterogeneity is linked to survival and thus some prognosis tool might be created with the described workflow. Moreover, describing intratumoral heterogeneity has been difficult using histopathology, and this approach could complement it.

An approach based on the molecular image's features was used to generate a model that integrates intensity, number of objects, and average surface per object for each *m/z* value. This workflow was implemented in a semi-automatic manner. This was used to describe a mouse kidney and tumor and to identify some *m/z* of interest. The extension of this approach to the comparison of individual *m/z* images was demonstrated in this study.

The focus of this study was on the first two cases presented in Figure 1. However, the proposed approach can be applied to all cases presented in Figure 1. Some particularly interesting parameters would be those allowing the automatic determination of whether a *m/z* follows a central or a peripheral distribution (e.g., for drug penetration in tumor), the average distance between objects (e.g., for glomerulonephritis diagnosis), and looking for specific shapes (e.g., astrocyte counting). The shape of the image could also be described to detect, for instance, epithelium presence in tissues.

Currently, no publicly available dedicated MSI software offers this kind of analysis out of the box. Some MSI software having segmentation workflows that give the classes' cardinalities (the number of spots in a class, i.e., disjointed region of interest) and more allow the export of a region of interest's spectra. Both would relate to the total surface of that region/class. It would benefit the community to validate this method by comparing its results to those of some targeted molecular staining.

The current workflow allows a higher extraction level of information from MSI datasets than what is currently done. This workflow can be used to complement most analyses. This information is quantitative and can be used to define pathology profiles with multiple parameters in order to, for example, define models of different tumor grades or tumor progression for diagnostics or prognostics purposes. Moreover, this workflow should be usable in processing and be applicable to other MSI techniques such as secondary ion mass spectrometry or inductively coupled plasma mass spectrometry, and in 3D (with an adjusted connexity) as well as 2D.

Acknowledgments

The authors thank Bruno Gomes from iTeos Therapeutics for allowing them to work on their samples, and Fabien Pamelard for the work done on making the datasets readable. The authors also thank Lauranne Poncelet for the constructive feedback.

Compliance with ethical standards

Conflict of Interest Gaël Picard de Muller, Rima Ait-Belkacem, David Bonnel, and Jonathan Stauber are employees of ImaBiotech SAS. *Research involving animals*: All animal experiments were compliant with the 2010/63/UE European Directive on Laboratory Animal Welfare and were approved by an Ethical Committee (Animal Welfare Body from the BUC CMMI Animal Facility in Gosselies, Belgium,. Animal Welfare Body Agreement number: LA 15005-18, Research Project Agreement number: BUC 2016-02, and BUC 2015-05).

References

1. Floros, D.J., Petras, D., Kapono, C.A., Melnik, A.V., Ling, T.J., Knight, R., Dorrestein, P.C.: Mass spectrometry based molecular 3D-cartography of plant metabolites. Front. Plant. Sci. **8**, 429 (2017)
2. Caprioli, R., Farmer, T., Gile, J.: Molecular imaging of biological samples: localization of peptides and proteins using MALDI-TOF MS. Anal. Chem. **69**, 4751–4760 (1997)
3. Römpp, A., Spengler, B.: Mass spectrometry imaging with high resolution in mass and space. Histochem. Cell Biol. **139**, 759–783 (2013)
4. Crecelius, A.C., Schubert, U.S., von Eggeling, F.: MALDI mass spectrometric imaging meets "omics": recent advances in the fruitful marriage. Analyst. **140**, 5806–5820 (2015)
5. Gorzolka, K., Kölling, J., Nattkemper, T.W., Niehaus, K.: Spatio-temporal metabolite profiling of the barley germination process by MALDI MS imaging. PLoS One **11**, 1–25 (2016)
6. Galli, M., Zoppis, I., De Sio, G., Chinello, C., Pagni, F., Magni, F., Mauri, G.: A support vector machine classification of thyroid bioptic specimens using MALDI-MSI data. Adv. Bioinformatics, **2016**, 3791214 (2016)
7. McDonnell, L.A., van Remoortere, A., van Zeijl, R.J., Deelder, A.M.: Mass spectrometry image correlation: quantifying co-localization. J. Proteome Res. **7**, 3619–3627 (2008)
8. Lagarrigue, M., Lavigne, R., Tabet, E., Genet, V., Thomé, J.P., Rondel, K., Guével, B., Multigner, L., Samson, M., Pineau, C.: Localization and in situ absolute quantification of chlordecone in the mouse liver by MALDI imaging. Anal. Chem. **86**, 5775–5783 (2014)
9. Otsuka, Y., Satoh, S., Naito, J., Kyogaku, M., Hashimoto, H.: Visualization of cancer-related chemical components in mouse pancreas tissue by tapping-mode scanning probe electrospray ionization mass spectrometry. J. Mass Spectrom. **50**, 1157–1162 (2015)
10. Römpp, A., Guenther, S., Takats, Z., Spengler, B.: Mass spectrometry imaging with high resolution in mass and space (HR2 MSI) for reliable investigation of drug compound distributions on the cellular level. Anal. Bioanal. Chem. **401**, 65–73 (2011)
11. Balluff, B., Frese, C.K., Maier, S.K., Schöne, C., Kuster, B., Schmitt M, Aubele, M., Höfler, H., Deelder, A.M., Heck, A., Hogendoorn, P.C., Morreau, J., Altelaar, A.F., Walch, A., McDonnell, L.A.: De novo discovery of phenotypic intratumou heterogeneity using imaging mass spectrometry. J. Pathol. **235**, 3–13 (2015)
12. Alexandrov, T., Bartels, A.: Testing for presence of known and unknown molecules in imaging mass spectrometry. Bioinformatics. **29**, 2335–2342 (2013)
13. Heijs, B., Abdelmoula, W.M., Lou, S., Briaire-de Bruijn, I.H., Dijkstra, J., Bovée, J.V., McDonnell, L.A.: Histology-guided high-resolution matrix-assisted laser desorption ionization mass spectrometry imaging. Anal. Chem. **87**, 11978–11983 (2015)

14. Collan, Y.: Morphometry in pathology: another look at diagnostic histopathology. Pathol. Res. Pract. **179**(2), 189–192 (1984)
15. Baatz, M., Zimmermann, J., Blackmore, C.G.: Automated analysis and detailed quantification of biomedical images using Definiens Cognition Network Technology. Comb. Chem. High Throughput Screen. **12**(9), 908–916 (2009)
16. Sahoo, P.K., Soltani, S., Wong, A.K.C.: A survey of thresholding techniques. Comput. Vis. Graph. **41**, 233–260 (1988)
17. Soille, P.: Morphological image analysis: principles and applications. Springer Verlag Berlin Heidelberg, New-York (2004)
18. Haralick, R., Shanmugam, K.: Textural features for image classification. IEEE Trans. SMC. **6**, 610–621 (1973)
19. Kassner, A., Thornhill, R.E.: Texture analysis: a review of neurologic MR imaging applications. Am. J. Neuroradiol. **31**(5), 809–816 (2010)
20. Yezzi, A., Kichenassamy, S., Kumar, A., Olver, P., Tannenbaum, A.: A geometric snake model for segmentation of medical imagery. IEEE Trans. Med. Imaging. **16**, 199–209 (1997)
21. Brattain, M.G., Strobel-Stevens, J., Fine, D., Webb, M., Sarrif, A.M.: Establishment of mouse colonic carcinoma cell lines with different metastatic properties. Cancer Res. **40**, 2142–2146 (1980)
22. Hunter, J.D.: Matplotlib: a 2D graphics environment. Comput. Sci. Eng. **9**, 90–95 (2007)
23. Smith, C.A., O'Maille, G., Want, E.J., Qin, C., Trauger, S.A., Brandon, T.R., Custodio, D.E., Abagyan, R., Siuzdak, G.: METLIN: a metabolite mass spectral database. Ther. Drug Monit. **27**, 747–751 (2005)
24. O'Rourke, M.B., Djordjevic, S.P., Padula, M.P.: The quest for improved reproducibility in MALDI mass spectrometry. Mass Spectrom Rev. 2016 Jul 15. doi: 10.1002/mas.21515.
25. Longuespée, R., Casadonte, R., Kriegsmann, M., Pottier, C., Picard de Muller, G., Delvenne, P., Kriegsmann, J., Pauw, E.: MALDI mass spectrometry imaging: a cutting-edge tool for fundamental and clinical histopathology. Proteomics Clin. Appl. **10**, 701–719 (2016)